A linear least-squares version of the algorithm of mode isolation for identifying modal properties. Part II: Application and Assessment

Matt Allen and Jerry H. Ginsberg

G. W. Woodruff School of Mechanical Engineering

Georgia Institute of Technology

Atlanta, GA 30332-0405

October 28, 2003

Running title: Algorithm of mode isolation. II: Assessment

ABSTRACT

The latest modifications of the Algorithm of Mode Isolation (AMI) for identification of modal properties from frequency response data are tested with synthetic data derived from an analytical model of an elastic frame in which flexure and torsion are coupled. The parameters of this model are selected to cause the occurrence of localized modal patterns in two modes having close natural frequencies. The response data is contaminated with white noise at a level sufficient to almost mask the two close modes. Results for the real and imaginary part of the eigenvalues are tabulated. The analytical modal patterns of displacement and torsional rotation are depicted graphically, accompanied by the discrete values obtained from AMI. Excellent agreement is found to occur for each mode, other than one of the pair of close modes. The poorer quality of that mode's identified properties is shown to be a consequence of its localized modal pattern. Results for the eigenvalues obtained by the rational fraction polynomial algorithm, which is an alternative modal identification technique, are found to be substantially less accurate as a consequence of difficulty in the presence of noise.

I. INTRODUCTION

Part I[1] described an iterative procedure that extracts the modal properties of a vibratory system from measured frequency response data. The procedure is called the Algorithm of Mode Isolation (AMI) because its primary feature entails isolating a single mode's contribution to each FRF. The first effort[2] was founded on a classical undamped modal representation of an FRF. A formulation fitting FRFs to a damped modal description was described subsequently[3,4]. The new features of AMI developed in Part I were its implementation of linear least squares for all aspects of parameter identification. The present paper examines AMI's performance under conditions where modal identification is known to encounter difficulty.

One faces a philosophical dilemma in deciding how to assess any algorithm for experimental modal analysis. Response data can be derived from an analytical model and then contaminated by a standard noise model. Using such data as the input to the algorithm leaves no ambiguity as to what the modal parameters should be, for they are available from the analytical model. However, such a line of investigation does not address how the algorithm would perform when applied to actual measured response data, where the noise might not fit a standard model, and where non-random errors may be present. The problem with using actual measured data is that there is no way of knowing exactly what the actual modal properties are, because ideal features, such as a clamped end condition for a beam, cannot be reproduced exactly, and prediction of dissipation effects from first principles is beyond present capabilities for built-up systems. It is for this reason that the present effort uses synthetic data derived from an analytical model.

Any modal analysis algorithm can be expected to have the most difficulty in systems that

3

have close natural frequencies, weakly excited modes, and low signal-to-noise ratios in their measured data. Prior works have used relatively simple systems to examine the accuracy of AMI in the presence of these problematic features. The initial effort[2] used data derived from a four-degree-of-freedom system with substantial non-proportional damping. That system had previously been used by Roemer and Mook[5] to test a modification of Juang and Suzuki's frequency domain eigenvalue realization algorithm[6].

The next model used to test AMI was a cantilevered beam with three suspended spring-mass-dashpot systems[3,4]. This system was a simplified version of one used by Strasberg and Feit[7] to examine energy transfer between structural components. In addition to permitting exploration of the role of noise, the small size of the suspended masses caused two modes to have natural frequencies that were closer than their bandwidths. This led to modal coupling, which refers to the merger in an FRF of resonance peaks that otherwise would be distinct. The small size of the suspended masses also led to a pair of modes that are weakly excited, and therefore readily masked by noise. (In fact, as will be evident here, high damping, close natural frequencies, and high noise levels mingle in their effect.) One consequence of tuning the subsystems to give the desired modal properties was that the first four modes were well separated from the high-frequency modes, which substantially simplfied the identification task. The performance of AMI for this model was assessed solely by comparing its predictions to the analytical modal properties. It was found that AMI worked well at identifying the natural frequencies and modal damping ratios, even in the presence of substantial additive white noise. However, it was found that some normalized mode vectors could not be found because they were weakly excited.

The need to improve the identification of weakly excited modes led to Zaki's modification of AMI[8], in which identification of the normal mode coefficients was deferred until the natural frequencies and modal damping ratios had been determined. The data he used to test this reformulation was synthesized from an analytical model of a frame composed of two orthogonally welded cantilevered beams loaded out-of-plane, which couples flexure and torsion. One reason for using this model is that many modes are required to describe its response. Also, the system parameters were adjusted such that mode coupling occurred. Various levels of white noise were added to test the limits of AMI, but the sole assessment criterion for AMI's performance was how well it identified the analytical modal properties.

The exposition in Part I incorporated Zaki's modification, as well as a linear least squares routine for extracting the eigenvalues from the FRF data. The objective here is to assess the performance of this latest version of AMI. The data to be analyzed is obtained from Zaki's elastic frame model. An additional measure beyond comparison with the analytical modal properties will be a comparison of AMI's values to those obtained by the Rational Fraction Algorithm first proposed by Richardson and Formenti[9], and then modified by many investigators, as detailed by Formenti and Richardson[10] in order to improve the algorithm's numerical stability and accuracy.

The frame structure presented here is the same as that used by Zaki, who formulated the system equations using Ritz series. However, further examination of that analysis revealed that the series diverged because of a poor choice of the Ritz basis functions. The model development presented here corrects this. However, it should be noted that after Zaki reduced the model to a finite number of degrees of freedom, all subsequent work depended only on

that reduced order model. Consequently, the modal identification was consistent with the erroneous analytical modal properties, and Zaki's findings regarding AMI were consistent.

The frame's parameters in the present work are adjusted such that two modes have close natural frequencies, and sufficient damping is introduced to cause modal coupling. Furthermore, these close modes display patterns of displacement and rotation that are localized to one span, and the degree to which flexure and torsion are coupled generally varies strongly between modes. Hence, there is a large variation in FRF magnitudes at various peaks.

II. ELASTIC FRAME PROTOTYPE

The parameters of an exercise offered by Ginsberg[11] are adjusted to obtain a system in which a pair of modes are coupled. It consists of two cantilevered beams that are oriented orthogonally and welded at their free ends, as depicted in Figure 1. Their junction has the effect of coupling the out-of-plane flexural displacement w and torsional rotation θ. Each beam has a solid circular cross section with 100 mm radius, modulus of elasticity $E = 70 \times 10^9$ Pa, modulus of rigidity $G = 26.32 \times 10^9$ Pa, and 2700 kg/m^3 density. The span lengths are set at $L_1 = 4$ m, $L_2 = 3.85$ m. Two transverse dampers, $c_1 = c_2 = 155.88$ N-s/m, oriented out-of-plane are placed at $x_1 = 4$ m and $x_2 = 3$ m. In addition, two torsional dampers, $c_3 = c_4 = 77.94$ N-s-m/rad, are placed at $x_1 = x_2 = 1$ m.

The span lengths were selected because they lead to two modes having close natural frequencies and modal patterns that are localized to one span, as will be seen. This occurs because $L_2 = L_1$ gives a symmetric system, so that setting L_2 slightly different from L_1 represents a small deviation from symmetry of a system consisting of weakly coupled components.

As described by Pierre, Tang, and Dowell,[12] one cause of mode localization is weak coupling between two energy depositories that deviate slightly from perfect symmetry. In the present system, the energy depositiories are the individual spans, and the coupling is provided by their welded connection. (An evaluation of the natural frequencies as a function of L_1 with $L_1 + L_2$ held fixed would show veering of the eigenvalue loci, which often accompanies mode localization, as shown by Chen and Ginsberg.[13]) Because the modes having close natural frequencies also have regions of low modal response, the selected values of L_1 and L_2 lead to a strong test of AMI's capabilities.

To construct an analytical model of the system the transverse deflection and torsional rotation of each beam are represented by Ritz series, with the associated Ritz coefficients serving as generalized coordinates for the system. The expansions for beam $n = 1$ or 2 are given by

$$w\left(x_n, t\right) = \sum_{j=1}^{N_R} \left(\Psi_w^{(n)}\right)_j \left(q_w^{(n)}\right)_j,$$

$$\theta\left(x_n, t\right) = \sum_{j=1}^{N_R} \left(\Psi_\theta^{(n)}\right)_j \left(q_\theta^{(n)}\right)_j$$

(1)

A similar model was constructed by Zaki[8] using monomial functions, but they lead to numerical problems due to ill-conditioning when the series length is increased beyond $N_R = 5$. For that reason, the eigenfunctions of a clamped-free beam are used as the basis functions for both beams. These are

$$\left(\Psi_w^{(n)}\right)_j = \sin\left(\alpha_j \frac{x_n}{L_n}\right) - \sinh\left(\alpha_j \frac{x_n}{L_n}\right)$$
$$- R_j \left[\cos\left(\alpha_j \frac{x_n}{L_n}\right) - \cosh\left(\alpha_j \frac{x_n}{L_n}\right)\right]$$
$$R_j = \frac{\sinh(\alpha_j) + \sin(\alpha_j)}{\cosh(\alpha_j) + \cos(\alpha_j)}$$

(2)

$$\left(\Psi_\theta^{(n)}\right)_j = \sin\left[\frac{(2j-1)\pi x_n}{2L_n}\right] \tag{3}$$

The response data presented here were obtained by truncating each series at $N_R = 11$. Bernoulli-Euler beam theory gives functionals describing the kinetic and strain energy in terms of w and θ, while the Rayleigh dissipation function depends on w and θ at the dashpot locations. Substitution of eqs. (1) into those expressions yields quadratic sums in the generalized coordinates or velocities. A similar operation applied to the virtual work yields the generalized forces. Lagrange's equations then leads to a set of $4N_R$ ordinary differential equations for the Ritz series coefficients.

The Lagrange equations do not couple the motion of the two beams. That effect is described by constraint conditions enforcing continuity of transverse displacement, and of rotation about the axis of each beam. It is required that

$$w(x_1 = L_1) = w(x_2 = L_2)$$
$$\left.\frac{\partial w}{\partial x_1}\right|_{x=L_1} = -\theta|_{x_2=L_2} \tag{4}$$
$$\left.\frac{\partial w}{\partial x_2}\right|_{x_2=L_2} = \theta|_{x_1=L_1}$$

Substitution of the Ritz series into the preceding leads to three algebraic constraint equations that supplement the $4N_R$ Lagrange equations. The unknowns are the Ritz series coefficients and three Lagrange multipliers. An elimination process based on solving the constraint equations for three generalized coordinates reduces the system to a set of $4N_R - 3$ differential equations. These equations may be solved through a state-space formulation for $8N_R - 6$ eigenvalues. Heavy damping would lead to overdamped modes marked by pairs of real eigenvalues. The more usual case is underdamped modes, which correspond to pairs of complex conjugate eigenvalues. This is the situation for all modes of the present system, so

8

there are $4N_R - 3$ complex modes.

Figure 2 displays the eigenvalue properties. In addition to displaying the undamped natural frequencies, $\Omega_k = |\lambda_k|$, and modal damping ratios, $\zeta_k = -\operatorname{Re}(\lambda_k)/|\lambda_k|$, the frequency difference, $\Omega_{k+1} - \Omega_k$, and the average bandwidth, $-\operatorname{Re}(\lambda_{k+1}) - \operatorname{Re}(\lambda_k)$ are plotted in order to assess the relative closeness of adjacent modes. As noted in the discussion in Part I, eq. (10), one can anticipate that the FRFs will exhibit mode coupling whenever the frequency difference $\Omega_{k+1} - \Omega_k$ is less than $-\operatorname{Re}(\lambda_{k+1}) - \operatorname{Re}(\lambda_k)$. This is the case for modes 8 and 9. Also notable is the wide range of damping ratios, which will be seen to significantly affect the data analysis.

The present work assesses AMI's performance when applied to synthetic FRF data describing the transverse displacement and torsional rotation at four locations on each beam: $x_1 = 1$, $x_2 = 2$, $x_3 = 3$, and $x_4 = 4$ m on beam 1 and $x_5 = 1$, $x_6 = 2$, $x_7 = 3$, and $x_8 = 3.85$ m on beam 2. Both beams have the same displacement at their junction. As a result, the data to be synthesized consists of fifteen impulse responses: seven displacements and eight rotations, which are grouped to form a vector according to

$$\{y(t)\} = [w_1\ w_2\ w_3\ w_4\ \theta_1\ \theta_2\ \theta_3\ \theta_4\ w_5\ w_6\ w_7\ \theta_5\ \theta_6\ \theta_7\ \theta_8]^{\mathrm{T}} \tag{5}$$

The FRF data will be a synthetic set mimicing an experiment in which a transverse impulsive force is applied at the first displacement point, so $P = 1$. The impulse responses are obtained analytically by employing a modal transformation that leads to a set of uncoupled equations for the modal generalized coordinates. The impulse response of a modal coordinate has the general form $\xi_k = C_k \exp(\lambda_k t)$, where λ_k are the modal eigenvalues and the participation factors C_k depend on the modal coefficients for the drive point. The modal

9

coordinates are evaluated at a uniform increment of time at a fixed sampling rate Δt within a window $0 \leq t \leq t_{\max}$, based on sampling criteria discussed later. The state-space modal transformation then yields a data set describing the history of the unconstrained set of Ritz series coefficients. Values of the full set of Ritz series coefficients are then obtained from the solution of the constraint equations. Finally, the impulse responses of the $\{y\}$ variables are obtained by synthesizing the Ritz series, eqs. (1). The same procedure when applied to the state-space eigenvector leads to the displacement pattern in any mode. Details of each step of this analysis are provided by Ginsberg[11].

The impulse response of each element of $\{y(t_n)\}$ is contaminated by white noise that is scaled relative to the peak magnitude of that variable, according to

$$y_j(t_n)_{\text{corrupt}} = y_j(t_n) + \alpha \max_n (y_j(t_n)) \, r_{jn} \tag{6}$$

where $-1 < r_{jn} < 1$ is a uniformly distributed random number and α is a constant that scales the random value to the required fraction of signal amplitude (0.02 for the data analyzed here). FFT processing of the contaminated impulse response data for each j yields the FRF $H_{jP}(\omega)$.

III.   RESULTS

The objective here is to assess the capability of AMI when the data has been sampled properly. Toward that end, the time window in which the impulse responses are sampled was set such that the slowest decaying complex modal coordinate reduced to an amplitude not exceeding 10^{-4} of its maximum. This is attained if $t_{\max} > \ln(10^4) / \min(|\text{Re}(\lambda_k)|)$. The sampling rate was set by the Nyquist criterion for the highest natural frequency, which

requires $\Delta t < \pi / \max \left(\left| \mathrm{Im} \left(\lambda_k \right) \right| \right)$. The values that were used are $t_{\max} = 14.2$ sec. and $\Delta t = 0.217$ ms, which corresponds to 2^{16} time values for each displacement variable. The frequency response data was truncated at $\omega = 3800$ rad/s, so the length of a frequency data set processed by AMI is 8589 samples.

As previously described, the excitation index is $P = 1$. Figure 3 shows $H_{11} \left(\omega \right)$, which is the noise-contaminated FRF at the drive point. Only seven resonant peaks are easily distinguished. For comparison, the noise-free analog in Figure 4 shows ten peaks. However, eleven modes have natural frequencies in the plotted frequency band. The discrepancy of each figure between the number of peaks and the number of in-band modes is readily explained. In the case of the analytical data, the expanded window shows only one peak in the vicinity of modes 8 and 9. The missing peak is a combination of coupling of these modes, and poor excitation of one of them, as will be seen. Figure 3 corresponds to superposition of white noise onto Figure 4. The level of this noise is comparable to the level of the resonant peaks above 2000 rad/s, resulting in masking of all high frequency peaks in the data to be processed by AMI.

To better understand the masking effect of noise consider the noise model invoked in eq. (6), in which the noise amplitude in the time domain is constant and scaled by the peak impulse response. In the frequency domain this represents white noise whose level in an FRF also is scaled proportionately to the peak amplitude of the corresponding impulse response. Because the noise level is essentially flat in frequency, the signal-to-noise ratio of $H_{jP} \left(\omega \right)$ in the vicinity of a resonance peak is set by the magnitude of the corresponding noise-free data. When the damping is light, so that $\left| \mathrm{Re} \left(\lambda_k \right) \right| \ll \mathrm{Im} \left(\lambda_k \right)$, a resonance is well approximated

11

as $\omega = \text{Im}\,(\lambda_k)$. Combining eqs. (4), (6) and (7) of Part I shows the peak FRF to be

$$(H_{jP})_{\text{peak}} \approx i\frac{\Phi_{jk}\Phi_{Pk}}{\zeta_k} \tag{7}$$

where U_{jk} is the kth modal coefficient for displacement j and ζ_k is the modal damping ratio. Thus, for a specified measurement point (fixed j) the modes k having the lowest peaks are those that are either the least responsive at the drive or measurement point, or most heavily damped. The normal mode functions for transverse displacement, which are presented later, decrease significantly with increasing frequency. Furthermore, Figure 2 shows that modes 8 and 9 are the most heavily damped, other than mode 1. Thus, the FRF contributions of the high-frequency modes may be expected in general to be masked to a greater extent, with the effect especially noticeable for modes 8 and 9.

The FRF for the torsional rotation at the drive point, $H_{51}\,(\omega)$, is depicted in Figure 5, while Figure 6 is the noise-free version. These present a different picture, in that ten peaks are evident even in the noisy data. Modes 8 and 9 are still coupled, but the torsional modal responses at $x = 1$ meter on the first beam is sufficient to exceed the added noise level. Careful examination of the enlarged view in Figure 6 shows that there is a slight dimple in the coupled peak, which suggests the presence of multiple modes, but this feature is completly masked by the noise. Most of the other FRFs are like Figure 3, in that the resonances above 2000 rad/s are masked. However, a few show one or more peaks in the upper frequency range. Typical of the latter is Figure 7, which depicts the torsional response at $x = 2$ meter on beam 2. Overall, the first seven modal peaks occur in each FRF, but the number of higher frequency modes that appear ranges between zero and three.

Application of the first two stages of AMI to each FRF yields multiple estimates of the

12

eigenvalues in the range below 3800 rad/s, at which the FRFs are truncated. Table 1 lists the number of eigenvalues and corresponding mode numbers obtained by processing each of the seven displacement FRFs and eight rotation FRFs. It is not surprising, given the fact that none of the FRFs display peaks at all eleven natural frequencies in this range, that in no case did processing an FRF give eleven eigenvalues. The first seven modes were identified in each FRF. For the closely spaced pair of modes, mode 8 was identified from a single FRF and mode 9 was identified in only three FRFs.

Except for modes 8 and 9, the magnitude of the analytical eigenvalues are quite distinct, as evidenced by Figure 2. In those cases, averaging like eigenvalues identified in each FRF is straightforward. In contrast, because of their closeness, merging the eigenvalue results for modes 8 and 9 poses a dilemma, especially if one divorces themself from analytical knowledge of the eigenvalue structure. The difficulty arises because no single FRF yielded both eigenvalues. Thus, these modes are a manifestation of the earlier discussion as to whether eigenvalues obtained from different FRFs should be averaged or kept distinct. The results obtained from the four FRFs giving λ_8 or λ_9 are listed in Table 2. One indication that the value obtained from FRF 5 does not belong to the values obtained from FRFs 12 to 14 is the fact that its real part deviates significantly from the other tabulated values. However, this difference is less than 25%, so it might be that the estimate from FRF 5 has a large error. Thus, consideration passes to the merger criterion in Part I, eq. (10). The values of $|\lambda|$ obtained from FRFs 12 to 14 are very close, so this criterion fails by a large margin, leading to the conclusion that they describe the same eigenvalue. In contrast, the largest average bandwidth using the tabulated λ from FRF 5 and any other FRF is 40.803 rad/s, while the

13

smallest corresponding natural frequency difference 19.649 rad/s. The merger criterion is (barely) met in this case, so the eigenvalue obtained from FRF 5 is taken to be distinct from the others.

The statistics of the averaged imaginary parts of the eigenvalues are provided in Table 3, while the corresponding information for the real parts appears in Table 4. The largest error in $|\text{Im}\,(\lambda_k)|$ relative to the analytical value is 0.4% for mode 8, but the average error for all modes is 0.04%. Also note that the 21.7% error for $\text{Re}\,(\lambda_8)$ is the largest, but the average error for all $\text{Re}\,(\lambda_k)$ is 3.7%. For both parts the standard deviation is a small fraction of the corresponding mean value, especially for modes 1 to 7, which means that there was little scatter in the individual values. Equation (4) in Part I converts the eigenvalues to modal natural frequency and damping ratio. The average errors are found to be 0.04% for frequency and 3.7% for the damping ratios. (The fact that these statistics are like those of the imaginary and real parts part of each eignevalue is is a consequence of the former being much larger and more accurate than the latter.) This represents a substantial improvement over the previous AMI algorithm. Zaki[8] reported 1.73% average error in natural frequency and 12.68% in damping ratio. (As described in the Introduction, the system used by Zaki was slightly different, so this is not a perfect comparison.)

The transverse displacement and torsional rotation for the seven lowest frequency modes are depicted in Figure 8; the abscissa is the distance along the centerline measured from the supported end of beam 1. Only the imaginary part of the mode function is displayed because the real parts of the mode functions are much smaller. For example, the most highly damped mode is the first, with a modal damping ratio of 0.0096. The ratio of the maximum

imaginary part to the maximum real part of the displacement in this mode is 120. This ratio is substantially higher for the other modes. (It can be proven that damped modal analysis of an undamped system will lead to purely imaginary eigenvectors that match the undamped modes. The dominance of the imaginary part of the modal displacement here is a consequence of the smallness of the overall damping level.)

The two spans are nearly equal, but it is easier to interpret the analytical modes if one first considers the case of equal span lengths. The modes then would be either symmetric or antisymmetric. The definition of positive w and θ for each span is such that a symmetric pattern would consist of a function for w that is even with respect to the midspan, while the function for θ is odd. Thus, the odd numbered modes in Figure 8 are comparable to the symmetric modes, and the even modes are like the antisymmetric modes. Increasing mode number is marked by an increase in the number of inflection points for w, but not for θ. This is a consequence of the fact that the beams are substantially stiffer in torsion than they are in flexure, so that the lower natural frequencies of the joined beams are well below the frequency at which either beam resonates in torsion.

It is evident that the first seven modes obtained from AMI are in close agreement with the analytical values. Even the jump in the torsional rotation at the juncture of the beams is captured. The seven displacement data points used to synthesize the data for AMI give a good picture of the torsional rotation for each mode in Figure 8, and they adequately sample the displacement pattern in the first five modes.

Figure 9 indicates that there also is good agreement between AMI's identification and the analytical values of modes 10 and 11, although it is evident that the analytical modes have

been undersampled. This figure also shows that the differences between the identified and analytical modal displacements are substantial for modes 8, while the discrepancies for mode 9 are less severe. Not shown is the fact that the AMI prediction for mode 8 has a real part that is not small compared to the imaginary part. Furthermore, the identified real part shows an irregular pattern for both displacement and torsional rotation. Modes 8 and 9 are the ones whose natural frequencies are close, with significant damping, but another factor also is responsible for the errors in the modes shapes. To recognize this consider the analytical mode functions. In mode 8 there is little displacement in the left span, $x < 4$ m, and little torsional rotation in the right span. This pattern is reversed for mode 9. Situations like this are recognized as mode localization phenomena, described by Pierre, Tang, and Dowell.[12]

The significance of the occurrence of mode localization lies in eq. (7). The excitation used to construct the present data set was a transverse force at $x = 1$ m on the first span. Examination of the displacement functions in Figure 9 shows that mode function 8 at $x = 1$ m is an order of magnitude smaller than mode function 9. Hence, the lower frequency mode is much more weakly excited. At most locations, the 8th modal response is masked by the noise, which is scaled by the maximum displacement at that location, or else it is dominated by the 9th modal response because of mode coupling. The one FRF from which mode 8 was identified was the torsional response at $x = 1$ m on the first span. Observe in Figure 9 that because of mode localization, the 9th modal response is very weak along this span, thereby leaving an opportunity for mode 8 to appear.

For comparison purposes, the noise-contaminated FRF data sets were analyzed using the rational fraction polynomial (RFP) method. This is an MDOF method in which an FRF is

16

represented as a ratio of polynomials in $(i\omega)$. Clearing the denominator leads to

$$H_{jP}(\omega)\sum_{k=1}^{2N} b_k\,(i\omega)^k = \sum_{k=1}^{2N-1} a_k\,(i\omega)^k \tag{8}$$

When this expression is evaluated at many frequencies where the FRF value is known, the result is a set of linear equations for the a_k and b_k coefficients that are solved in a least-squares sense. The eigenvalues and residues are readily obtained from these coefficients. The RFP version that was implemented follows the development provided by Maia *et al*,[14] including the application of orthogonal polynomials. This version concurrently processes all FRFs, thereby leading to a single global estimate of the eigenvalues. However, computer memory limitations made it necessary to process a limited amount of data at once, so the system order was restricted to not exceed ten. For the same reason, the full frequency range was decomposed into three bands that contained modes 1-5, 6-7, and 8-11. These restrictions also served to avoid ill-conditioning in the numerical analysis.

Because RFP requires an initial guess as to the number of participatory modes, computations within each frequency band were carried out with a range of guesses up to a maximum of ten. A stabilization chart[15] was constructed to identify which modes were consistently identified. Figure 10 shows the stabilization chart for the frequency band containing modes 8-11. Like AMI, this implementation of RFP had the greatest difficulty in this range. The marks in the chart indicate the frequencies, $|\lambda_k|$ identified by RFP for each model order from three to ten. The FRF that accompanies these values is a composite obtained by adding the absolute value of the eleven individual FRFs at each frequency. It serves to pictorially indicate where natural frequencies might reside. At each peak no consistent pattern is observed, with the scatter at the second and third peaks being quite substantial. Also, the

17

apparent convergence to an eigenvalue at 3800 rad/s should be ignored because it is at the limit of the frequency band. Note that there is no system order at which the stabilization chart indicates the presence of two modes in the vicinity of 2500 rad/s, where modes 8 and 9 are situated.

Because of the limitation on the system order, no consistent pattern was recognized. For this reason, the RFP results discussed here are for the model order that yielded estimated natural frequencies closest to the analytical values. For the lower and upper frequency bands the best results were obtained when the system order was set to nine, while a system order of six gave the best results for modes 6 and 7. For the first seven modes, RFP showed an average error in $\text{Im}(\lambda_k)$ of 0.22%, with a worst case of 1.2% for mode 1. The corresponding errors for $\text{Re}(\lambda_k)$ were 7.1 % average, with a worst case error of 24.8% for mode 2. Mode 8 was not detected at all by RFP. For modes 9 to 11, the average error of $\text{Im}(\lambda_k)$ was 0.68%, with a worst case of 1.36% for mode 11. Mode 11 also had the largest error for $\text{Re}(\lambda_k)$, at 60%, while the average error of $\text{Re}(\lambda_k)$ for these modes was 24%. These statistics are substantially worse than those for AMI, as described by Tables 3 and 4. Also, AMI did succeed in identifying mode 8.

IV.   SUMMARY AND CONCLUSIONS

The performance of the linear-least-squares version of AMI was tested with synthetic data derived from an analytical model of an elastic frame formed by joining two cantilever beams at right angles. The frame is loaded out-of-plane, so the welded connection couples flexure and torsion. The synthetic response data were derived by using Ritz series to represent

18

the transverse displacement and torsional rotation. The temporal response to a transverse impulse force at the quarter-point of one span was obtained by applying state space modal analysis. The impulse responses of the Ritz coefficients were discretely sampled, and used to synthesize the transverse displacement and torsional rotation at eight cross-sectional locations. Each impulse response was contaminated be adding uniformly distributed random noise. The data then was FFT processed to produce FRFs that were input to the modified AMI. Generally, the best signal-to-ratios are obtained at resonance peaks, which are the regions from which AMI selects the data for its numerical fits. However, the manner in which the white noise was scaled resulted in masking the higher frequency resonance peaks in most FRFs.

The span lengths of the model were selected to be nearly equal, which resulted in the occurrence of a pair of modes, 8 and 9, having close natural frequency and modal patterns that are localized to one span. The damping of these modes was sufficient to cause the individual resonant peaks to merge, in the phenomenon known as modal coupling. The role of noise was magnified by the localized nature of these modes, which weakened the modal excitation of one and the modal response of the other.

The frequency band that was processed contained eleven modes. AMI identified the first seven modes when each of the fifteen FRFs were processed, but the higher frequency modes were sparsely identified because their contribution to an FRF was masked by the added noise. The close localized modes 8 and 9 were the most difficult to identify. Mode 8 was identified from only one FRF, while mode 9 was found from three FRFs. The eigenvalue of mode 8 showed the greatest discrepancy with the analytical value. Its imaginary part, which

is analogous to the damped natural frequency for proportionally damped systems, had an error of 0.4%, while its real part, which is the negative of the modal decay rate, was 21.7% in error. The corresponding average errors for all eleven modes were 0.04% for the imaginary part and 4% for the real part.

The analytical mode shapes were depicted by plotting the transverse displacement and torsional rotation dependence on the distance along the cross-section centerline. The discrete modal displacements and rotations extracted by AMI were overlaid onto the analytical graphs. The agreement was quite good, except for mode 8. The main features of the first five modes were clearly discernible from the discrete pattern identified by AMI. However, the higher frequency modal patterns were undersampled because the locations selected for the FRF data were too sparsely spaced. The error encountered in mode 8 was substantial, and indicated that the mode was not essentially imaginary, which is unlike the corresponding analytical mode function. The primary source of the lower quality of this mode's identification was shown to be a combination of relatively high damping and low modal response at the drive point.

An alternative identification of the eigenvalues was also carried out using a global version of the rational fraction polynomial (RFP) algorithm. RFP requires an *a priori* guess as to the number of participitory modes. A range of guesses was used to identify the system order giving the best results. The average and worst case errors for both parts of the eigenvalues were found to be substantially larger than the errors encountered with AMI. Also, RFP did not identify mode 8. In a separate computation, not reported here, RFP was applied to the noise-free FRFs. This yielded excellent agreement for all eigenvalues, including that for

mode 8. This observation suggests that RFP is more sensitive to noise than is AMI.

The results presented here indicate that the current version of AMI algorithm is capable of accurate system identification in the presence of extreme noise and modal coupling. At the same time, modes that are weakly excited were found to be more difficult to identify, because they were barely discernible relative to the noise floor. In this sense, AMI is like other techniques that process response data derived from a single excitation. One can anticipate that extension of AMI to process simultaneously response data obtained from several excitations might address this shortcoming.

ACKNOWLEDGEMENT OF SUPPORT

References

[1] J. H. Ginsberg and M. Allen, "A linear least-squares version of the algorithm of mode isolation for identifying modal properties. Part I: Conceptual development," submitted (2003).

[2] M. V. Drexel and J. H. Ginsberg, "Mode Isolation: A new algorithm for modal parameter identification," J. Acoust. Soc. Am. **110**, 1371-1378 (2001).

[3] M. V. Drexel and J. H. Ginsberg, "Modal parameter identification using state space mode isolation," Proc. 19th International Modal Analysis Conference, Orlando, FL, 2001.

[4] M. V. Drexel, J. H. Ginsberg, and B. R. Zaki, "State space implementation of the algorithm of mode isolation," J. Vib. Acoust. **125**, 205-213 (2003).

[5] M. J. Roemer and D. J. Mook, "Enhanced realization/identification of physical modes", J. Aero. Eng. **3**, 122-136 (1990).

[6] J. N. Juang and H. Suzuki, "An eigensystem realization algorithm in frequency domain for modal parameter identification", J. Vib., Stress, Rel. in Design **110**, 24-29 (1988).

[7] M. Strasberg and D. Feit, "Vibration damping of large structures induced by attached small resonant structures", J. Acoust. Soc. Am. **99**, 335-344 (1996).

[8] B. R. Zaki, *A Modified Approach to Improve the Robustness of the Algorithm of Mode Isolation.* Ph.D. thesis, Georgia Institute of Technology, Atlanta, GA (2002).

[9] M. H. Richardson, and D. L. Formenti, "Global curve-fitting of frequency response measurements using the rational fraction polynomial method," Proc. 3rd International Modal

Analysis Conference, Orlando, FL, 1985.

[10]D. Formenti and M. H. Richardson, "Parameter estimation from frequency response measurements using rational fraction polynomials (twenty years of progress)," Proc. 20th International Modal Analysis Conference, Los Angeles, CA, 2002.

[11]J. H. Ginsberg, *Mechanical and Structural Vibrations: Theory and Applications* (John Wiley and Sons, NY, 2001) Chap. 9.

[12]C. Pierre, D. M. Tang, and E. H. Dowell, "Localized vibrations of disordered multi-span beams: theory and experiment," *AIAA J.* **25**, 1249-1257 (1987).

[13]P.-T. Chen and J. H. Ginsberg, "On the relationship between veering of eigenvalue loci and parameter sensitivity of eigenfunctions," *J. Vib. Acoust.* **114**, 141-148 (1992).

[14]N. M. M. Maia, J. M. M. Silva, J. He, N. A. J. Lieven, R. M. Ling, G. W. Skingle, W.-T.To, and A. P. V. Urgueira, *Theoretical and Experimental Modal Analysis and Testing* (Research Studies Press Ltd., Taunton, Somerset, England, 1997) Chap. 4.

[15]R. J. Allemeng and D. L. Brown, "A unified matrix polynomial approach to modal identification," J. Sound Vibration **211**, 301-322 (1998).

| Displacement | Identified modes | |
data set	#	Indices
(1) w_1 @ $x_1 = 1$	7	1-7
(2) w_2 @ $x_1 = 2$	7	1-7
(3) w_3 @ $x_1 = 3$	7	1-7
(4) w_4 @ $x_1 = 4$	7	1-7
(5) θ_1 @ $x_1 = 1$	10	1-8, 10,11
(6) θ_2 @ $x_1 = 2$	9	1-7, 10,11
(7) θ_3 @ $x_1 = 3$	7	1-7
(8) θ_4 @ $x_1 = 4$	9	1-7, 10,11
(9) w_5 @ $x_2 = 1$	7	1-7
(10) w_6 @ $x = 2$	7	1-7
(11) w_7 @ $x_2 = 3$	7	1-7
(12) θ_5 @ $x_2 = 1$	10	1-7, 9,10,11
(13) θ_6 @ $x_2 = 2$	9	1-7, 9,10
(14) θ_7 @ $x_2 = 3$	9	1-7, 9,10
(15) θ_8 @ $x_2 = 3.85$	8	1-7,10

Table 1: Modes identified by processing each set of displacement data. (Maximum number of modes is 11.).

FRF #	Eigenvalue
5	$-22.876 \pm 2490.838i$
12	$-17.927 \pm 2510.592i$
13	$-17.153 \pm 2511.112i$
14	$-17.221 \pm 2510.661i$

Table 2: Identified eigenvalues for the 8th and 9th modes obtained by processing individual FRFs.

	$\left| \text{Im} \left(\lambda \right) \right|$		
Mode number	Analytical value	Mean	Standard deviation
1	68.008	68.005	0.0072
2	265.912	265.913	0.0022
3	386.325	386.332	0.0200
4	829.452	829.452	0.0008
5	1033.752	1033.754	0.0276
6	1697.012	1697.013	0.0047
7	1937.890	1937.912	0.0695
8	2479.743	2490.838	0.0000
9	2511.042	2510.788	0.2305
10	2995.661	2995.853	0.3833
11	3380.042	3380.367	0.4793

Table 3: Statistics of the identified natural frequencies.

	$-\operatorname{Re}(\lambda)$		
Mode number	Analytical value	Mean	Standard deviation
1	0.6565	0.6557	0.0080
2	0.1640	0.1641	0.0011
3	0.4826	0.4836	0.0040
4	0.2670	0.2670	0.0010
5	0.7935	0.7929	0.0146
6	0.6107	0.6115	0.0028
7	3.1205	3.0668	0.1123
8	18.7961	22.8759	0.0000
9	18.1254	17.4338	0.3496
10	5.3462	5.0665	0.5277
11	5.2109	4.7864	0.6445

Table 4: Statistics of the identified modal decay rates.).

List of Figures

Figure 1: L-shaped frame cantilevered at both ends with attached dashpots.
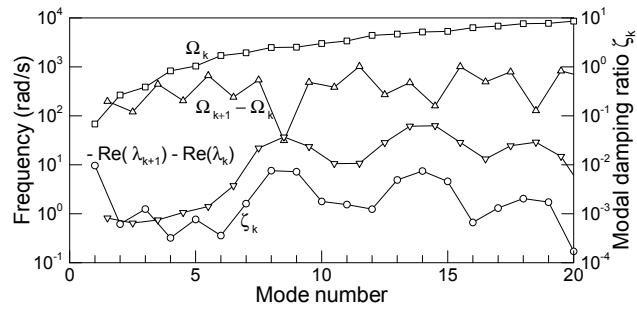
Figure 2: Natural frequencies, modal damping ratios, frequency differences, and average modal bandwidths for the first twenty modes of the frame.
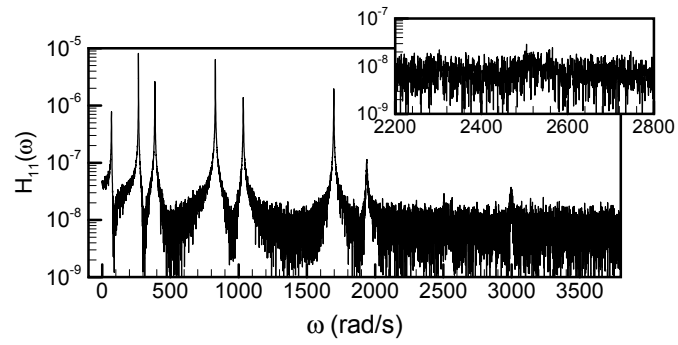
Figure 3: Noise contaminated displacement FRF at $x = 1$ m on beam 1.
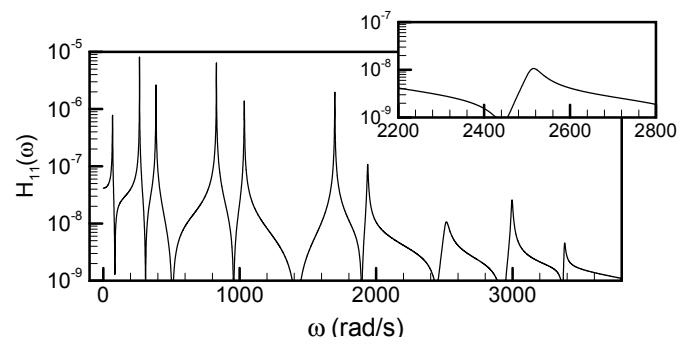
Figure 4: Noise-free displacement FRF at $x = 1$ m on beam 1.
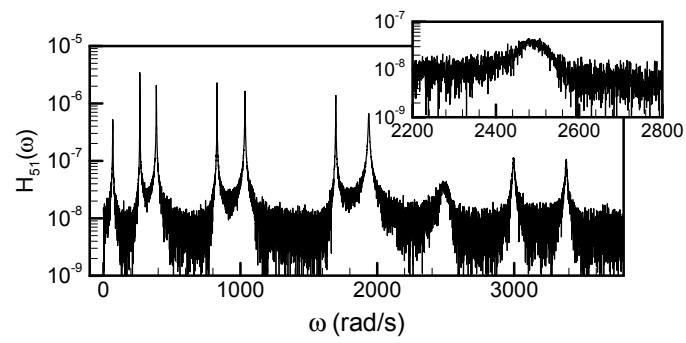
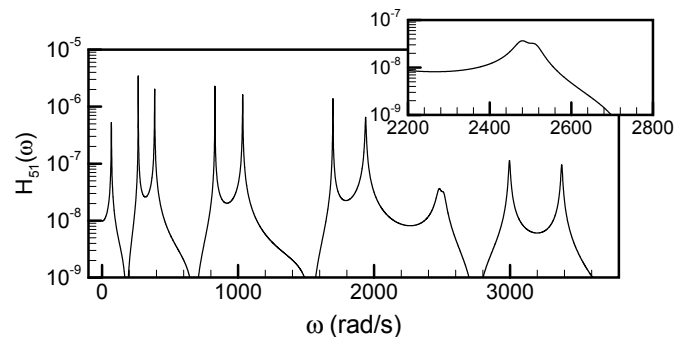Figure 5: Noise contaminated rotation FRF at $x = 1$ m on beam 1.
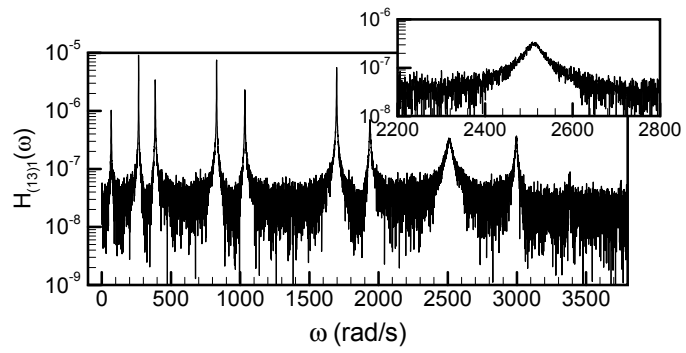
Figure 6: Noise-free rotation FRF at $x = 1$ m on beam 1.

Figure 7: Noise contaminated rotation FRF at $x = 2$ m on beam 2.
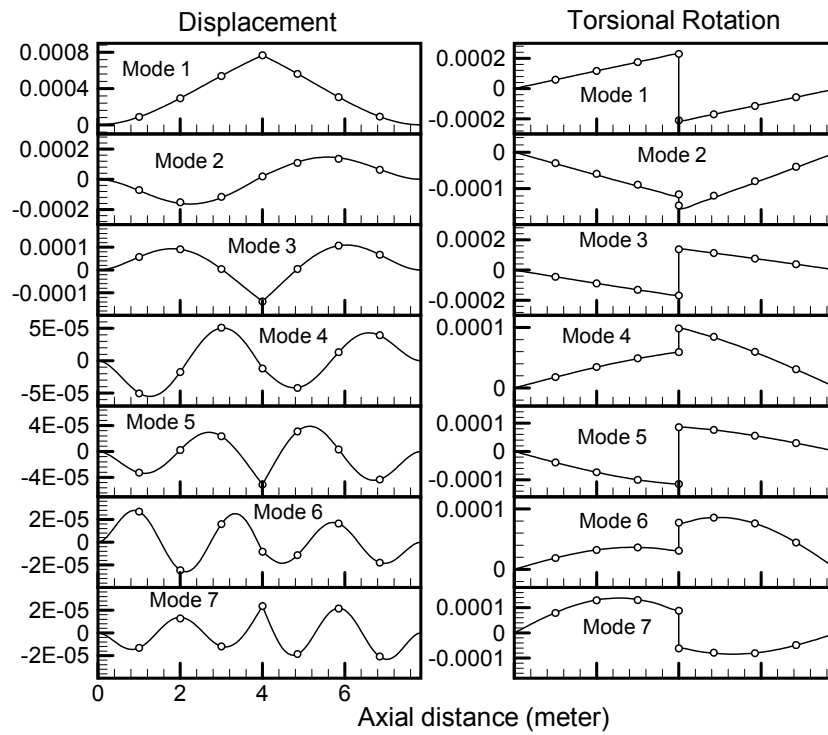
Figure 8: Imaginary part of the modal amplitudes, modes 1-7; analytical value: ——, identified by AMI: ○.
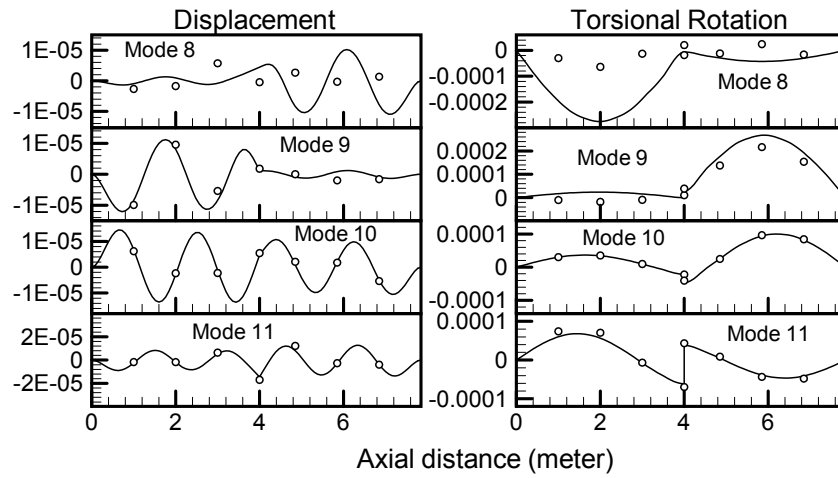
Figure 9: Imaginary part of the modal amplitudes, modes 8-11; analytical value: ——, identified by AMI: ∘.
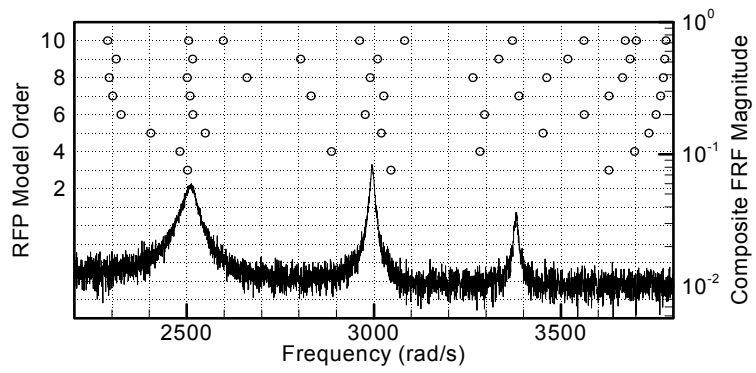
Figure 10: Stabilization chart corresponding to results from the RFP alogorithm for a range of model orders. $\text{Im}\left(\lambda_k\right)$ obtained from RFP: $\circ$, composite FRF: ——.